ADVANCED ELECTRONIC MATERIALS Open Access
www.advelectronicmat.de

From Plant Oils to High-Performance Supercapacitor Electrode: Poly(guaiazulene) via Photopolymerization

Sena Ermis, Sinem Altinisik, Fahri Catoglu, Yusuf Yagci, Erdem Sari, Steffen Jockusch, Sermet Koyuncu,* and Kerem Kaya**

Due to the increasing global demand for electrical energy, the fabrication of advanced energy storage devices, such as supercapacitors (SCs), with outstanding performance is of paramount importance. Herein, the facile light-induced synthesis of a conjugated conductive polymer, namely, poly(guaiazulene) (PGz) is reported on, using a naturally available, low-cost monomer, guaiazulene (Gz). PGz and PGz_rGO (obtained by combining PGz with reduced graphene oxide (rGO)) exhibited high-performance supercapacitor (SC) electrode properties, including remarkable specific capacitance (52.75 F g^{-1} at 0.24 A g^{-1} and 258.6 F g^{-1} at 5.00 A g^{-1}, respectively), excellent cycling stability (97.1% and 94.0% stability after 5000 cycles), high power density (95.5 and 2118.8 W kg^{-1}), and, most importantly, high energy density (5.81 and 30.57 Wh kg^{-1}). These superior features are attributed to the hierarchical porous nature and high electrical/ionic conductivities of the photochemically obtained PGz. Contrary to previous techniques that require harsh reaction conditions, such as carbonization and coupling reactions, the reported photopolymerization involves solely the irradiation of an ethyl acetate solution of a Gz-organic photoinitiator (2-bromoacetophenone) mixture. The photochemical synthesis described here provides a powerful method to produce a sustainable and high-performance SC electrode material, offering a great alternative to commercial SCs.

1. Introduction

The rapid evolution of electric cars, airplanes, and optoelectronic devices has led to a significant rise in the global demand for advanced energy storage devices.[1] Supercapacitors (SCs), also called ultracapacitors or electrochemical capacitors, have recently gained significant interest due to their superior power density (≈8 kW kg^{-1}), longer lifespan (>100.000 cycles), and faster charging time (1–10 s) compared to the existing metal ion battery technologies (mainly Li-ion batteries (LIBs) with ≈150 W kg^{-1} power density, 500–1000 cycles, 2–3 h of charging time).[2] SCs can store much more energy than conventional capacitors and can supply this energy with higher power outputs than LIBs, bridging the gap between conventional capacitors and LIBs. Today, SCs are found in many applications that require rapid charge/discharge ability, such as photographic flashes, portable speakers, electric/hybrid vehicles, electric screwdrivers, defibrillators, and some optoelectronic devices.[3]

One major drawback of the SCs is their limited delivery of energy density (up to 10 Wh kg^{-1} versus 300 Wh kg^{-1} of LIBs) which severely restricts their wide application in many other technologies.[4] SCs consist of four components; electrode material which is the key part, current collector, electrolytes, and separator that prevent physical contact, thus, preventing

S. Ermis, Y. Yagci, K. Kaya
Department of Chemistry
Istanbul Technical University
Maslak, Istanbul 34469, Türkiye
E-mail: kkaya@itu.edu.tr

S. Altinisik, F. Catoglu, S. Koyuncu
Department of Chemical Engineering
Canakkale Onsekiz Mart University
Canakkale 17100, Türkiye
E-mail: skoyuncu@comu.edu.tr

S. Altinisik, F. Catoglu, S. Koyuncu
Department of Energy Resources and Management
Canakkale Onsekiz Mart University
Canakkale 17100, Türkiye

E. Sari
Chemistry Department
Gebze Technical University
Gebze, Kocaeli 41400, Türkiye

S. Jockusch
Center for Photochemical Sciences
Bowling Green State University
Bowling Green, OH 43403, USA
E-mail: jockus@bgsu.edu

The ORCID identification number(s) for the author(s) of this article can be found under https://doi.org/10.1002/aelm.202400570

DOI: 10.1002/aelm.202400570

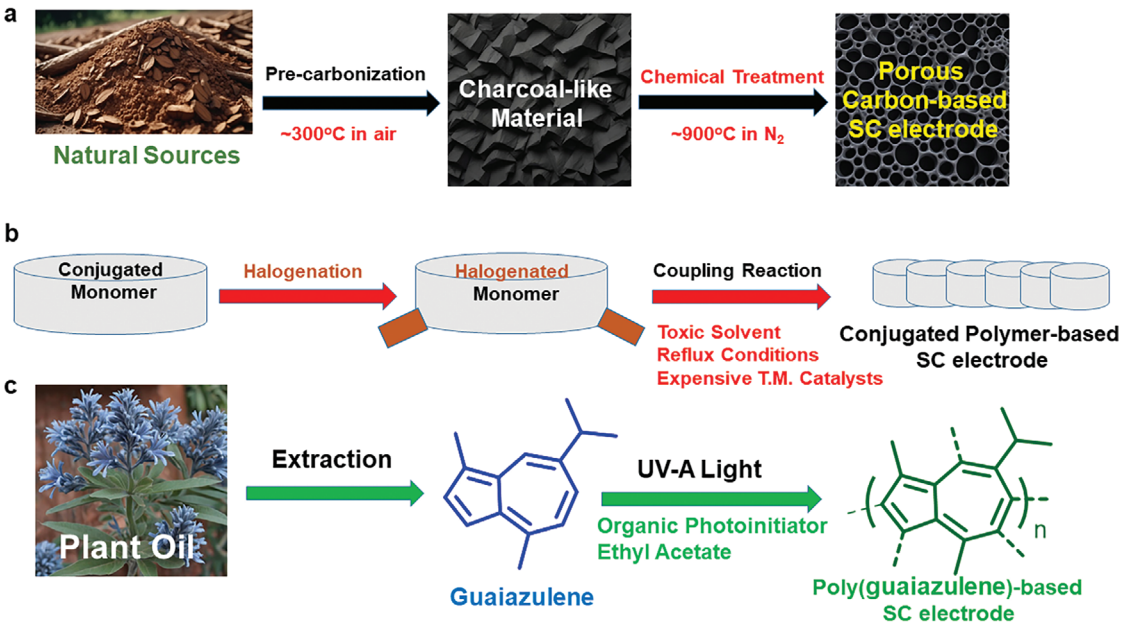

Figure 1. Different pathways leading to supercapacitor (SC) electrode materials for SC electrodes. a) Carbonization methods generating carbon-based SC electrodes. b) Coupling Methods leading to CCP-based SC electrodes and c) Reported photopolymerization method leading to poly(guaiazulene)-based SC electrode.

short-circuiting of the electrodes. Great efforts have been dedicated to improving the energy density of SCs while maintaining their high power density. [5] This way, next-generation SCs are believed to be utilized as standalone batteries.[6] In order to obtain high energy density in SCs, it is crucial to fabricate new electrode materials with specific properties. Accordingly, an ideal electrode should have the following key characteristics: i) a porous structure with a vast pore size distribution for the high accessibility of electrolytes ii) good electrical/ionic conductivities, and iii) low production cost.[7]

SC electrodes are generally categorized into three groups. The first group is the electric double-layer capacitors (EDLCs), which store charges via Coulombic static charge adsorption/desorption. The second group is the pseudocapacitors and they store charges by using fast Faradaic redox reactions in a wide potential range. The last group is the hybrid SCs which combine the features of both EDLCs and pseudocapacitors by taking advantage of both kinds of storage mechanisms, providing both high power and high energy densities.[8]

A wide variety of materials, including metal oxides,[9] transition metal carbides/nitrides (MXenes),[10] carbon-based materials,[11] conjugated conductive polymers [12] and metal–organic frameworks (MOFs),[13] have been extensively investigated as SC electrodes. Carbon-based materials, e.g. porous (activated) carbon, graphene,[14] carbon nano-tubes,[15] and fullerenes have been explored as promising SC electrodes.[16] Among these carbon-based materials porous carbon, due to its low cost, high porosity, chemical/thermal stability, and high electrical/ionic conductivity, is recently regarded as the most promising material and is currently used in commercial SCs as the only electrode material.[17] Commercial SCs contain porous carbon electrodes with pore diameters of ≈1–2 nm which are used in conjunction with aqueous/organic salt electrolytes. Porous carbon is either obtained by hydrothermal treatments [18] or by the carbonization [19] (slow pyrolysis) process of a wide variety of carbon-based substances, yielding charcoal-like materials (**Figure 1a**). Previous studies have demonstrated that fine tailoring of the reaction conditions is necessary to control the porosity of the final material.[20]

Conjugated conductive polymers (CCPs) are emerging as the best alternatives to carbon-based SCs since they are flexible (important for wearable technologies), environmentally benign, and easy to functionalize.[21] The performances of CCP-based electrodes rely on their chemical and morphological features in the nanoscale, which depend on their macroscale production methods.[22] A great variety of conjugated heteroaromatic polymers, e.g., polypyrrole, polyaniline, polythiophene and its derivatives (especially poly 3,4-ethylenedioxythiophene (PEDOT)) have been utilized as promising SCs.[23] On the other hand, their homoaromatic counterparts, namely, conjugated polycyclic aromatic hydrocarbons (PAHs), notably, polypyrene, polynaphtalene, and polyazulene, despite their superior planarity, extended $\pi-$surface, and better thermal/chemical resistances, have scarcely been synthesized and investigated.[24–28] This is mainly attributed to their poor solubility, the difficulty of their functionalization, and their higher costs.[29] A great majority of the synthetic methods for CCPs involve the employment of coupling reactions which require long-time refluxing of the halogenated monomers in toxic organic solvents in the presence of expensive transition metal catalysts (Ni (0) and Pd (0)) (Figure 1b).[30]

Recently, there has been a significant shift towards sustainability among scientists due to serious environmental concerns, with the aim of minimizing both energy and environmental costs.[31] The ultimate goal is to use mild reaction conditions and

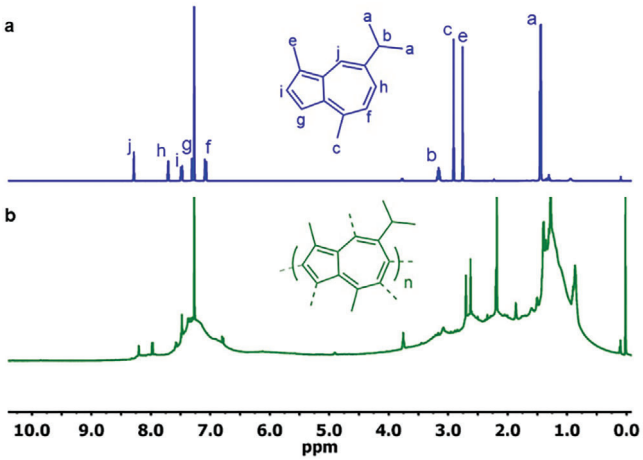

Figure 2. ^{1}H NMR spectra of a) Gz and b) PGz measured in CDCl3 at 500 MHz.

environment-friendly/green and cheap compounds for the fabrication of technologically important devices.[32] Hence, there is a growing interest in the preparation of porous carbon-based SCs using natural compounds such as lignin,[33] chitosan,[34] argan shell,[35] tannins,[36] water spinach,[37] bio-oils and bio-chars.[38] However, all the above-mentioned hydrothermal or carbonization treatments for the synthesis of carbon-based SCs and coupling reactions for the synthesis of CCP-based SCs require high temperatures and/or corrosive/expensive chemicals, contradicting the concept of sustainability.

In the realm of sustainable chemistry, light-induced polymerization (photopolymerization) reactions stand as the best option, since they require little or no solvent and use light of different wavelengths, as the sole energy source, minimizing the energy requirements.[39–43] In addition, photopolymerization reactions have the advantage of spatiotemporal control, a crucial phenomenon for 3D-printing applications enabling the fabrication of materials with precise architectures.[44] Regarding the application of photopolymerization methods for the synthesis of organic CCPs, the Kalow research group has published noticeable works regarding the light-induced chain-growth polymerization of n-type monomers.[45] On the other hand, our research group has recently reported the light-induced step-growth polymerization of different p-type heteroaromatic and homoaromatic monomers generating industrially important polymers such as PEDOT [46] and its co-polymers,[47,48] polythiophene derivatives,[49] poly(*N*-ethylcarbazole),[50,51] poly(*N*-methylpyrrole),[52] poly(*N*-methylindole),[42] and polypyrene,[53] respectively.

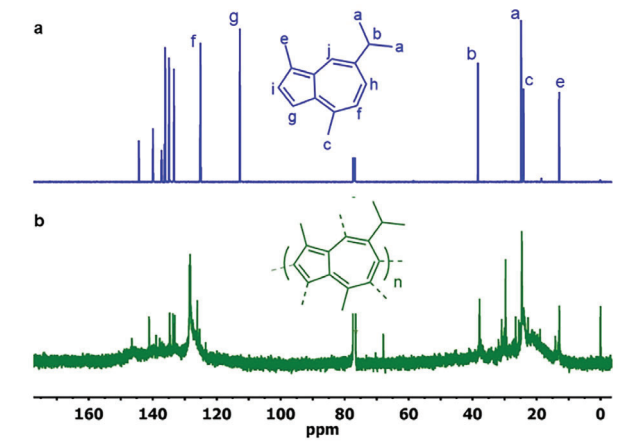

Figure 3. ^{13}C NMR spectra of a) Gz and b) PGz measured in CDCl3 at 125 MHz.

Guaiazulene (Gz), a naturally occurring alkyl derivative of azulene (1,4-dimethyl-7-isopropylazulene) is an abundantly available PAH (found in many plant species). It serves as a promising and cost-effective alternative monomer, with a cost ≈100 times lower (≈\$5 g^{-1}) than azulene.[54] Despite being widely utilized in various cosmetic and beauty products, such as skin care creams, hair dyes, toothpaste, and eye solutions, as an FDA-approved non-toxic substance,[55] there appears to be limited research on its polymerization. Best to our knowledge, only a single study has addressed its polymer, namely, poly(guaiazulene) (PGz).[56] However, this study reported the occurrence of PGz in oligomeric form, consisting of five to six repeating units. Nevertheless, these oligomers displayed promising optoelectronic features.

Driven by our previous light-induced step-growth polymerization of conjugated monomers [46–53] and by the possibility of using a natural, cheap organic monomer (Gz) as a sustainable resource for the fabrication of advanced energy storage devices, herein, we report for the first time, on the light-induced synthesis and characterization of near-infrared (NIR) absorbing PGz with outstanding SC electrode features (Figure 1c). The superior electrode properties of PGz are attributed to its high electrical/ionic conductivities and its homogeneous nanoporous structure with vast pore size distribution. The evidenced doped nature of PGz is responsible for the electrical/ionic conductivities. The reported method involves the UV-A irradiation of the ethyl acetate solution of Gz and phenacyl bromide (PAB) rendering the advanced system energetically much more efficient and sustainable than the conventional carbonization or coupling methods.

2. Results and Discussion

2.1. Light-Induced Synthesis of PGz

PGz was synthesized by adapting a previously employed reaction procedure for the light-induced synthesis of PEDOT.[46] Details of the reaction procedure can be found in the Experimental Section of the Supporting Information. In short, equimolar amounts of Gz and PAB were dissolved in ethyl acetate (EtAc) solvent and then irradiated at room temperature using a UV-A light-emitting photoreactor for 24 h. Then, the solution was precipitated into 10-fold cold diethyl ether to remove unreacted Gz, PAB, and acetophenone (side product). The resultant dark green colored polymer was then dried under vacuum at room temperature for 24 h.

2.2. Synthesis of Dedoped PGz

Chemical dedoping is a well-known neutralization procedure to remove the dopant ions using mostly diamines, acting as strong

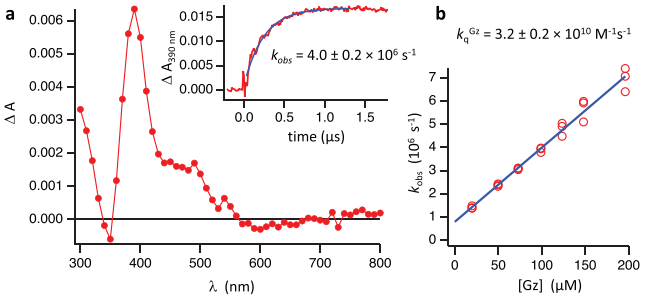

Figure 4. a) Transient absorption spectrum of PAB (10 m) in the presence of Gz (0.1 mM) in deoxygenated acetonitrile solutions recorded at 0.5–1.5 μs after the laser pulse (355 nm, 7 ns pulse width) The inset shows the growth kinetic of the Gz radical cation monitored at 390 nm. b) Determination of the bimolecular rate constants kq_{Gz} of generation of transients at 390 nm. Pseudo-first order rate constant (k_{obs}) determined from the growth of the transient absorption at 390 nm versus varying concentrations of Gz.

reducing agents.[57] For the dedoping procedure, dark green PGz powder was initially poured into 100 mL methanol. Then, hydrazine monohydrate was added drop-wise while continuously stirring until the color of the solution turned from dark green to dark brown. Dedoped PGz was then dried under a vacuum for 24 h. Photos of Gz powder, PGz, and dedoped PGz powders can be seen in Figure S1 (Supporting Information).

2.3. Structural Characterization of PGz and Dedoped PGz

Initially, ^{1}H NMR (**Figure** 2a,b) and ^{13}C NMR spectra (**Figure** 3a,b) of Gz and PGz were measured to compare the spectra and examine polymeric species. The broadening of all the peaks in the spectra of PGz (both aliphatic and aromatic regions) (Figures 2b and 3b) is a clear indication of the successful polymerization. In addition, the disappearance of the peak at 112 ppm and a significant decrease in the intensity of the peak at 125 ppm (Figure 3b) highlight the main connections (couplings) through 3-, 5- positions (g- and f-positions, respectively) of Gz units. The disappearance of the peak at 112 ppm indicates that head-to-head connection from -g carbon (3-position) is more dominant than head-to-head connection from -f carbon (5-position). This phenomenon is later discussed in the theoretical calculations and attributed to the sterically less hindered surrounding of carbon at -g position. Control experiments evidenced the crucial role of the combination of light and PAB since there was no spectral change (^{1}H NMR) in the absence of light (Figure S2, Supporting Information) or PAB (Figure S3, Supporting Information).

Table 1. Reaction details of the light-induced synthesis of PGz.

Monomer[a)]	Conversion [b)] [%]	M_w [c)] [kDa]	m/z [d)]	Đ [c)]	Polymer
Gz	52	2.19	2514	2.0	PGz

[a)] Photopolymerization reaction was performed in EtAc solvent at 355 nm nominal irradiation for 24 h. More details of the photopolymerization procedures can be found in the Supporting Information; [b)] Conversion was determined gravimetrically after drying the polymer under vacuum; [c)] Determined by GPC; [d)] Determined by MALDI-TOF.

Infrared spectra measurements of Gz, PGz, and dedoped PGz were also conducted to compare the differences (Figure S4, Supporting Information). While no significant changes were observed in the functional groups of the polymer, the drastic intensity increase observed ≈3370 cm^{-1} in the spectrum of PGz is attributed to the atmospheric water molecules (—OH stretching) interacting with dopant ions (bromide anions and radical cations) through ion-dipole interactions.[47] Significant changes were also present in the fingerprint regions of Gz and PGz (1300–800 cm^{-1}), indicating different C—C bonding (couplings) between the repeating Gz units. In the IR spectrum of dedoped PGz, due to the removal of the ions during the dedoping procedure, no significant peak corresponding to —OH stretching was present ≈3400 cm^{-1}.

Following the main spectral investigations (NMR and IR), the molecular weight of PGz was investigated by gel-permeation chromatography (GPC) (Figure S5, Supporting Information) and by matrix-assisted laser desorption-ionization time-of-flight (MALDI-TOF) spectroscopy (Figure S6, Supporting Information). **Table** 1 depicts the reaction conditions, weight-average molecular weight (M_w), and dispersity (Đ) of PGz together with the monomer conversion and reaction details for the light-induced polymerization of Gz. The mass spectrum (Figure S6, Supporting Information) exhibits the presence of polymeric species having m/z ≈2515 representing ≈13 repeating Gz units each separated by m/z ≈200. Compared to the previously obtained PGz, via GZ oxidation by $FeCl_3$ vapor, the much larger number of repeating Gz units was observed using both gel-permeation chromatography (GPC) and MALDI-TOF (5–6 vs 12–13). Additionally, the mass spectrum displays oligomers (dimer,

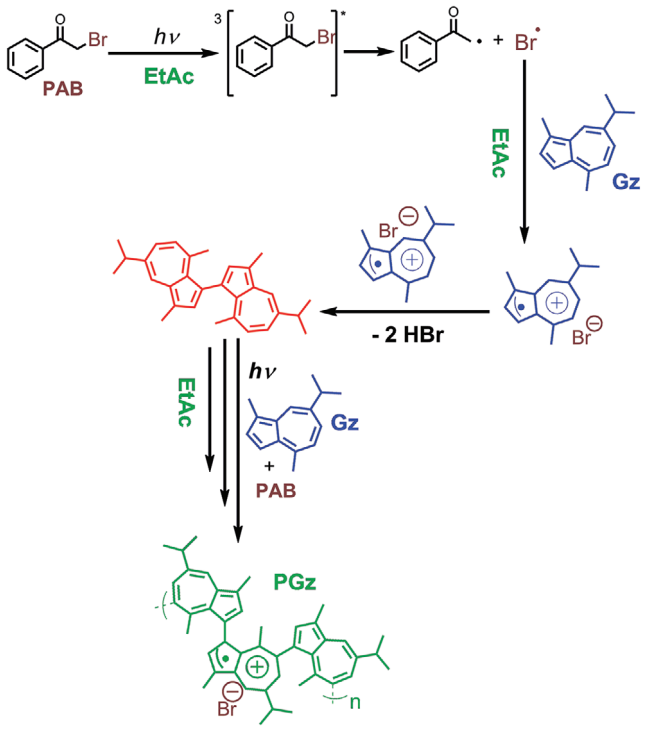

Figure 5. Proposed reaction mechanism of the light-induced polymerization of Gz leading to PGz.

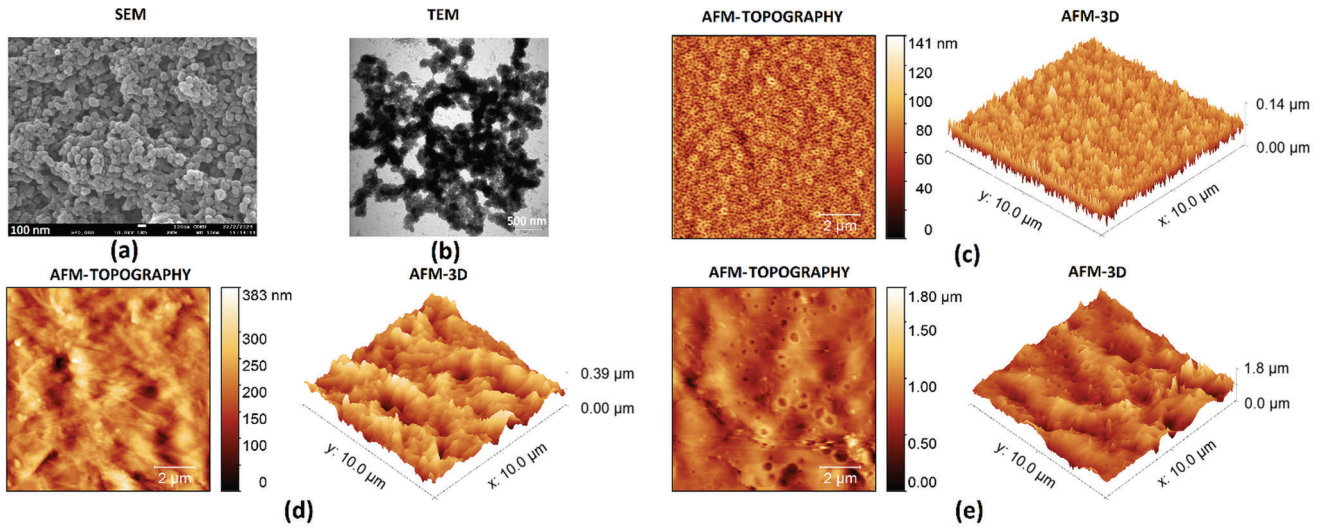

Figure 6. Morphological Images of PGz. a) SEM. b) TEM images of PGz powder. c) AFM images of the pristine PGz film on a glass surface. d) PGz film on graphite sheet. e) PGz_rGO film on graphite sheet.

trimer, and tetramer) with the highest intensities along with higher molecular weight polymeric species with lower intensities. These data are in good coherence with the mass spectrum of poly(*N*-ethylcarbazole) obtained using a similar photopolymerization method [50] and evidence once again the step-growth nature of the reported polymerization method. The absence of any peak(s) representing brominated species (51:49 ratio of intensity due to 79-Br and 81-Br isotopes) or phenacylated species (+106 m/z) confirms that the photoinitiator didn't take part in the termination step of the reported light-induced polymerization reaction.

As mentioned in the introduction part, good electrical/ionic conductivities are the key factors for the superior performance of any SC electrode. Electrical/ionic conductivities of PGz and dedoped PGz were measured using a four-point probe and an ionic conductometer, respectively at room temperature and 50% RH. While PGz exhibited an electrical conductivity of 0.14 mS cm^{-1}, its dedoped analogue had a conductivity of only 1 µS cm^{-1}. This expected result in the dedoped PGz is attributed to the removal of charges (removal of radical cations and bromide ions) which are responsible for the electrical conductivity of PGz. Similarly, while different concentrations of aqueous PGz solutions displayed good ionic conductivities (Table S1, Supporting Information) reaching up to 3.72 mS cm^{-1}, developed PGz due to its insolubility in water did not display any ionic conductivity.

The crystallinity of the Gz monomer and PGz was evaluated by conducting powder X-ray diffractography (PXRD) (Figure S7, Supporting Information). Gz due to its already well-known crystallinity, exhibited sharp peaks.[58] On the other hand, PGz's diffractogram displayed a totally amorphous character with no sharp peaks and a single broad peak centered at 22° (2-theta). This is due to the strong $\pi-\pi$ stacking of the aromatic units corresponding to a distance of ≈4 Å.[59] Strong $\pi-\pi$ interactions in the solid state, are expected to result in excellent morphological properties that are crucial for improved ion transportation.[60]

To check the wettability of the monomer and the polymers (PGz and dedoped PGz) contact angle measurements were performed using pellets prepared using IR pellet system. Figure S8a (Supporting Information) shows the water contact angle results and Figure S8b (Supporting Information), photos of all contact angle measurements. Three angles during 1 min shot (each 20 s) were averaged. Accordingly, while Gz's water contact angle is 91.7° which makes Gz slightly hydrophobic, PGz's water contact angle is 56.1°, displaying hydrophilic character. This hydrophilicity is due to the presence of dopant ions which were also observed in the above measurements. On the other hand, dedoped PGz's water contact angle is 133.8° which renders dedoped PGz highly hydrophobic.

Laser flash photolysis experiments were performed to investigate the nature of the reactive species involved in the photopolymerization of Gz. Excitation of PAB in deoxygenated acetonitrile solutions with laser pulses of 355 nm yielded only weak transient absorption signals.[52] However, in the presence of 10 mM Gz the growth of a strong transient with a maximum at 390 nm was observed (**Figure 4a**). The transient was assigned to the Gz radical cation based on a spectrum of azulene radical cations reported in the literature.[61] The signal growth followed first-order kinetics with a rate constant of $k_{obs} = 4.0 \times 10^6$ s^{-1}. Variation of the Gz concentration (20–200 µM) revealed a strong dependence on the rate constant of the growth of the transient absorption of Gz radical cations. The plot of this rate constant (k_{obs}) versus the Gz concentration gave the bimolecular rate constant of generation of Gz radical cations ($kq_{Gz} = 3.2 \times 10^{10}$ M^{-1} s^{-1}) (Figure 4b).

Based on the laser-flash photolysis and spectroscopic data, a proposed reaction mechanism is depicted in **Figure 5**. Initially, through its excited triplet state, PAB photodecomposes under UV-A irradiation to phenacyl and bromine radicals. The highly reactive bromine radical accepts an electron from the Gz monomer forming Gz radical cation with bromide counter anion. Coupling of two Gz radical cations by the release of 2 moles of HBr acid form the Gz dimer. Further irradiation, oxidation by bromine radicals, and release of HBr by coupling reactions result in the formation of polymeric species in a step-growth fashion. Due to the presence of HBr in the system, the final polymers have

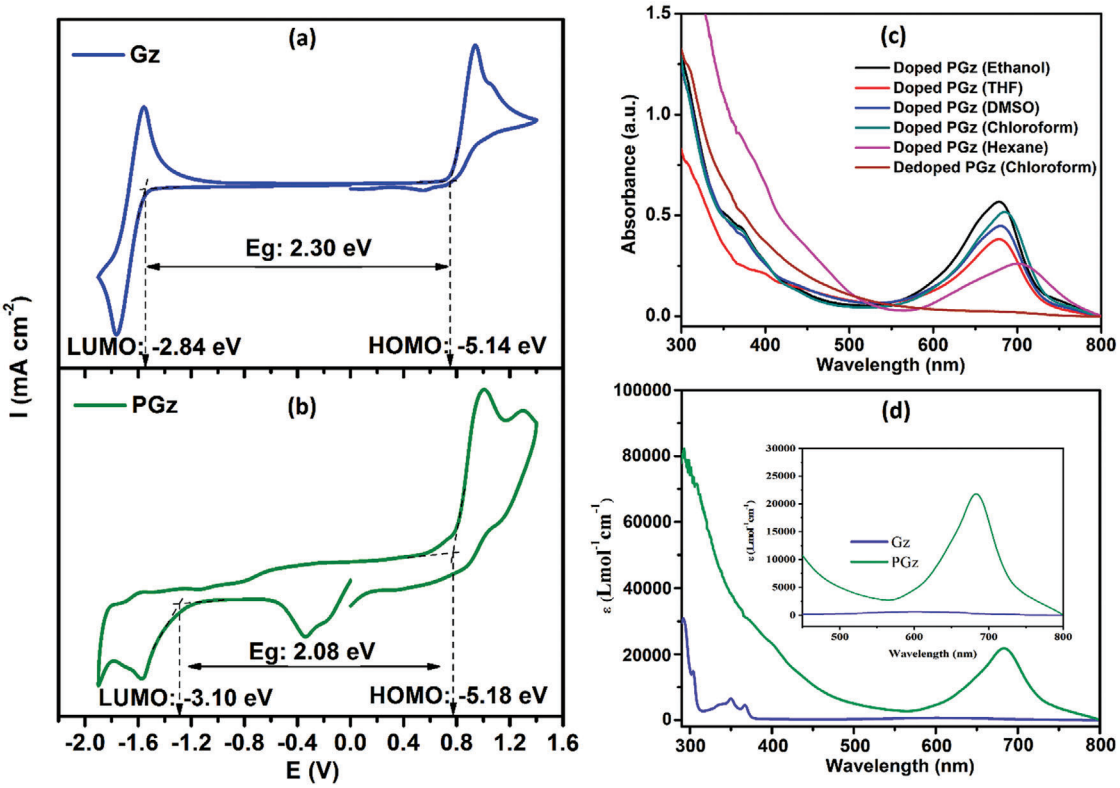

Figure 7. a) Cyclic voltammograms Gz and b) PGz in a 0.1 M TBAPF6/ACN electrolyte solution at a scan rate of 100 mV s^{-1} with Ag/AgCl. c) UV–vis spectra of PGz measured in various organic solvents and the spectrum of dedoped PGz (orange line) measured in chloroform. d) UV–vis spectra of Gz (blue line) and PGz (green line) measured in ethanol.

a doped nature since it is well-established that mixing of such Brønsted acids with con-jugated polymers forms conductive con-jugated polymers.[62]

Thermal gravimetric analysis (TGA) was conducted to get insights into the thermal stabilities of Gz, PGz, and dedoped PGz (Figure S9, Supporting Information). While PGz displayed thermal stability up to 104 °C (first 5% weight loss), dedoped PGz was thermally more stable and displayed the first 5% weight loss ≈170 °C. The main reason for the higher thermal stability of the dedoped PGz is due to the absence of dopant ions. Our previous works have demonstrated that bromide anions start to evaporate ≈150 °C.[50] At 800 °C, PGz has the highest char yield (47%). The higher char yield of PGz compared to dedoped PGz (43% char) is attributed to the slight degradation of the polymer during the dedoping procedure.[63]

Following the spectral and thermal characterizations, morphological properties of PGz were examined using scanning electron microscopy (SEM), transmission electron microscopy (TEM), and AFM (atomic force microscopy) (**Figure 6a–e**). In line with the PXRD data (Figure S6, Supporting Information) SEM data of PGz also revealed an amorphous morphology with interconnected pores (macro- and mesopores) (Figure 6a). In the SEM micrograph, the formation of aggregates composed of homogeneously distributed spheres with ≈100 nm radius was observed.

These spherical aggregates, supported by TEM images (Figure 6b), indicate a regular and repeatable structure of PGz, which ensures consistent physical properties that are important for ion transportation.

Moreover, the uniform distribution of interconnected pores enables the movement of electrolyte counter ions in the doping/dedoping process, which can ultimately result in an increase in capacitance.[64] Homogenous nanoporous structure helps to buffer volume changes during the charge/discharge process, thus, improving the cycling stability. AFM image of the pristine PGz film prepared via drop-casting (Figure 6c), exhibits a highly uniform distribution of PGz particles (RMS 11.15 nm) underpinning its application in energy storage devices. On the other hand, in the AFM image of the electrode prepared on a graphite sheet using PGz as a binder with PVDF: HFP (Figure 6d), a porous and undulating surface was observed, with slightly increased roughness value (RMS 16.52 nm). Upon addition of rGO to PGz, the AFM image (Figure 6e) of the similar electrode system showed expanded undulations and increased micro-level porosity (RMS 37.30 nm). PGz_rGO film on graphite sheet.

Nitrogen (N_2) physisorption isotherm analysis of PGz was performed at 77 K up to a pressure of 1 bar; the Brunauer–Emmett–Teller (BET) specific surface area (SSA) was measured as 22.3 m^2 g^{-1} with an average pore size of 4.6 nm (Figure S10, Supporting Information). The pore width distribution statistics demonstrate that PGz has a mesopore-dominated porous structure. It has been previously demonstrated that a hierarchical pore size distribution in which large pores surround smaller pores

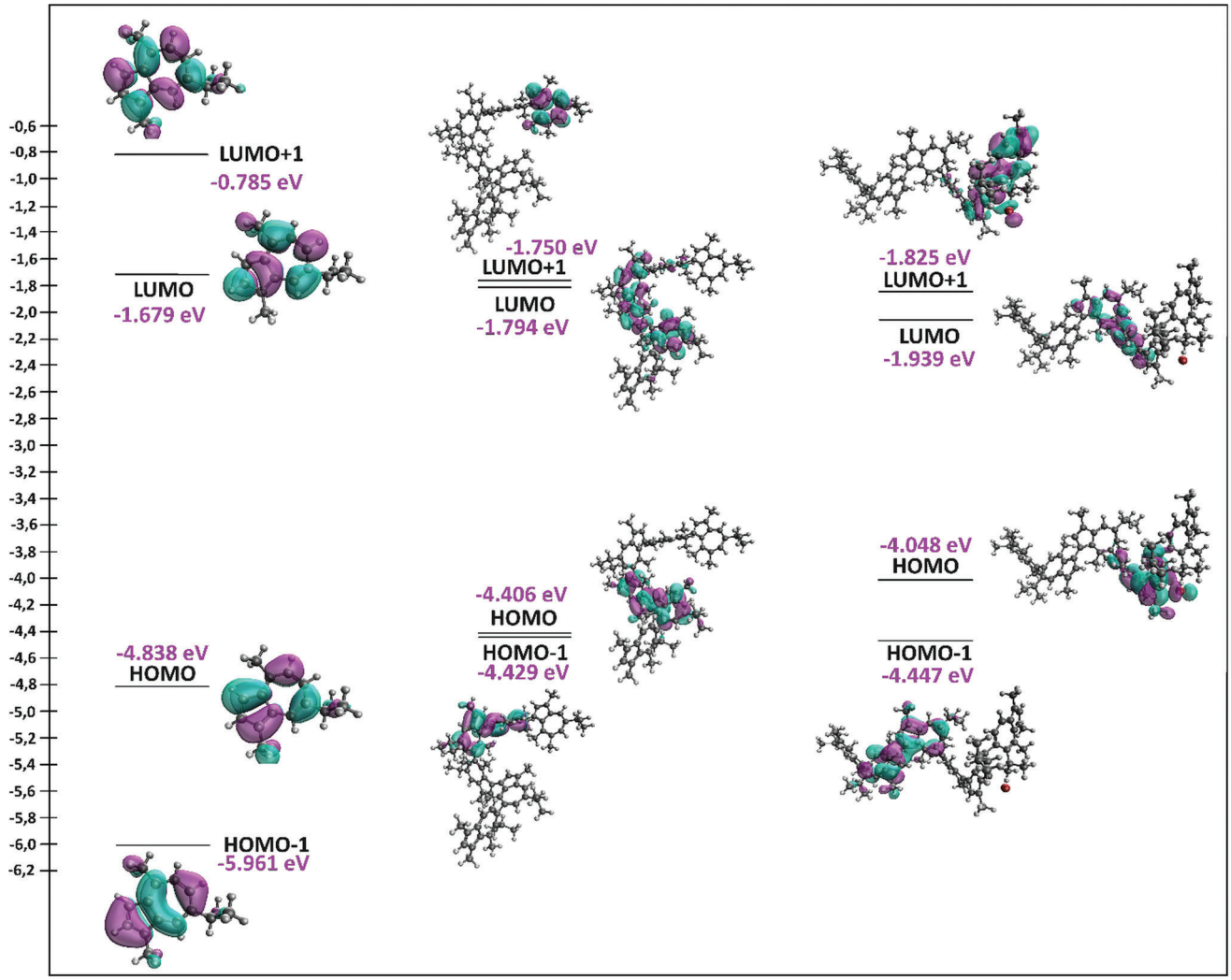

Figure 8. Theoretical HOMO-LUMO charge distribution and energy levels of Gz, dedoped PGz, and PGz at the B3LYP/6-31G (d,p) basis set, respectively.

results in a broad pore size distribution. In addition, mesopores (2–50 nm) are believed to facilitate the passage of electrolytes (ions) to micropores.[65] Compared to reported SCs, the relatively lower SSA of PGz is attributed to the close pack-aging due to the strong $\pi-\pi$ interactions observed in PXRD. While high SSA is considered as an important factor (especially for EDLC-type SCs),[66] porosity plays a more crucial role in the ion diffusion kinetics depending on the pore interconnectedness that would theoretically result in more pseudocapacitative character.[67]

The electrochemical properties of both monomer (Gz) and polymer (PGz) were investigated using cyclic voltammetry (CV) (**Figure** 7a,b). The reversible reduction peak observed in the cathodic scan ($E_{\_red}$ (m,a) = −1.66 V) is ascribed to the reduction of the bipolar behavior Gz ring.[68] In the anodic scan of the Gz monomer, the irreversible oxidation peak observed at 0.94 V is attributed to the condensed π-conjugated structure. After the aryl-aryl coupling reaction occurring during the polymerization process, the oxidation onset potential remained almost the same in PGz compared to the monomer due to the localization of charges within the repeating units. The first peak observed ≈ −0.33 V during the cathodic scan of PGz is attributed to the reduction of the charged (doped) structure formed as a result of polymerization. The second reduction was observed at a more negative potential (ca. −1.6 V) showing a partially positive shift and modification of the electrochemically reversible reduction behavior due to radical quenching, which results from the conjugated bond system.[69] According to all these CV results, the electrochemical bandgap values for Gz and PGz were found to be 2.30 and 2.08 eV, respectively.

In the comparison of the UV–vis absorption spectra of Gz and PGz (Figure 7c) a red shift of ≈100 nm (590 to 690 nm) observed in PGz is due to aryl-aryl coupling reaction resulting from the polymerization (extended conjugation) and also due to formation of guaiazulenium radical cations.[70] Previous studies have demonstrated a correlation between the ratios of cationic species and the intensity of the peak ≈690 nm, indicating a highly doped nature for PGz.[71] Much higher absorption observed between 400 and 500 nm, in the spectrum of PGz, is also attributed to the $\pi-\pi^*$ transition resulting from the formation of poly(guaiazulene). The UV–vis spectra of PGz in

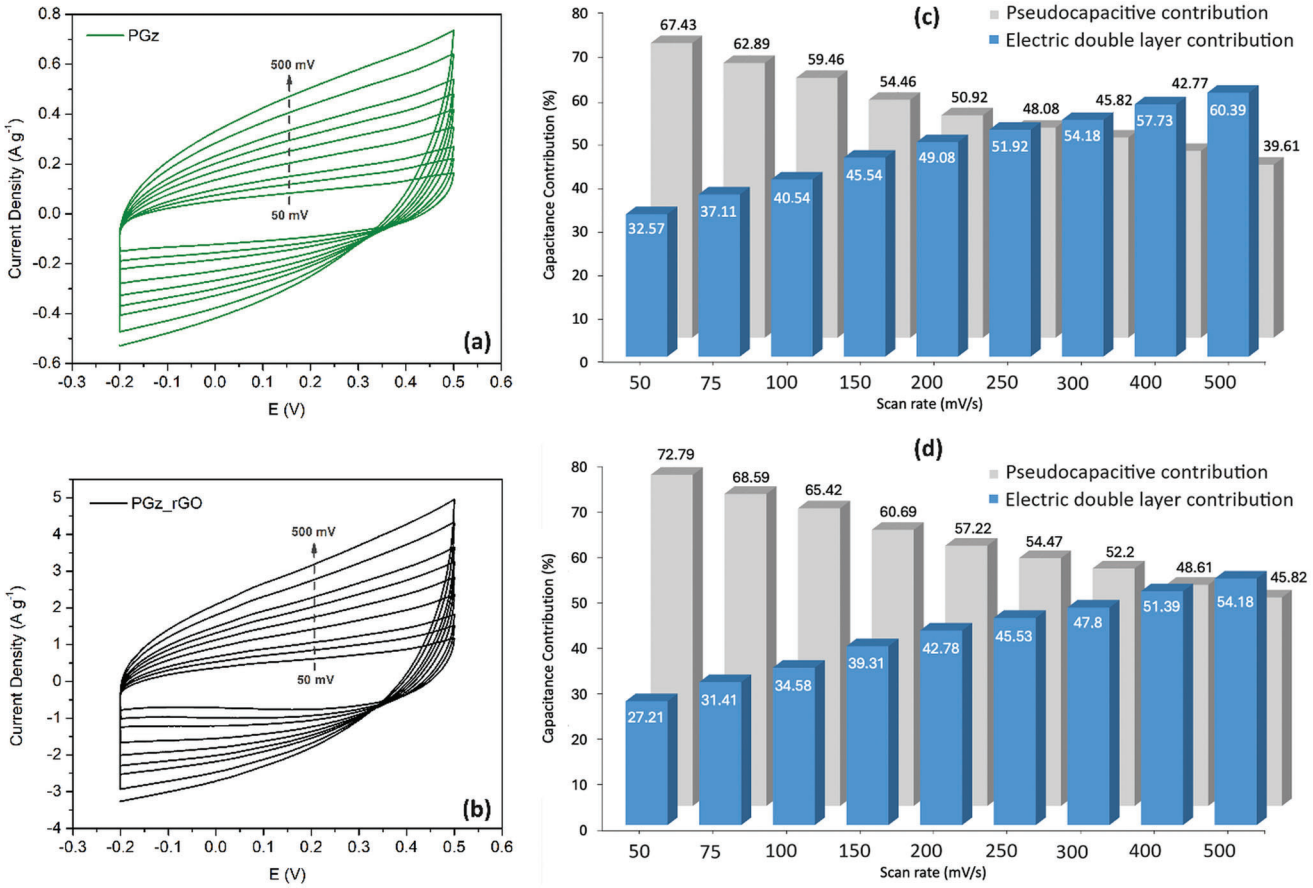

Figure 9. Cyclic voltammograms a) PGz electrode and b) PGz_rGO electrode. Percentage of EDL and pseudocapacitive behavior according to Dunn method at different scan rates and 0.15 V for c) PGz electrode and d) PGz_rGO electrode.

different solvents show large bathchromic shifts (Figure 7d) reaching the NIR region (≈750 nm), with molar absorptivity coefficients of ≈20 000 L $mol^{-1}cm^{-1}$ in ethanol solution. Theoretical calculations suggest that the positive net charges of the oxidized states in azulene and its derivatives are localized in the seven-membered ring.[72] Upon chemical dedoping, the band at ≈690 nm disappears, indicating neutralization.

Moreover, UV–vis data (Figure S11, Supporting Information) reveal that PGz has slight solubility in water (3 mg mL^{-1}), making it an attractive material also for various bio-applications. The water solubility of PGz is due to ion-dipole interactions between the dopant ions (radical cation and bromide) and polar water molecules. Both electrochemical and optical features of the photochemically obtained PGz strongly suggest that it can be utilized as a promising HTM, especially for organic electronics.[73]

Theoretical HOMO-LUMO charge distribution and energy levels of Gz, dedoped PGz, and PGz were calculated using the B3LYP/6-31G (d,p) basis set (**Figure 8**). Gz is an azulene derivative, characterized by its relatively high HOMO and low LUMO energy levels, attributed to its distinctive polarized structure.[74] Unlike azulene, the branched alkyl chains present in Gz, significantly improve solubility after polymerization. 3D structures of the monomer and possible polymeric structures in the Cartesian coordinate plane were supported by geometric optimization (Figure S12, Supporting Information). In this context, its 2D extended π-system around the core makes it an excellent candidate for hole transport components in solution-processed organic electronic devices.[62] 3- and 5- positions in the five and seven-membered rings of Gz, respectively, where polymerization mostly occurs, have large HOMO coefficients. The HOMO of Gz is distributed in odd-position carbon atoms, while the coefficients of the LUMO and the HOMO-1 are larger in even-position carbon atoms. On the other hand, in the possible dedoped PGz structure, it is observed that charges are localized on the seven-membered rings at the HOMO, while at the LUMO, they are distributed across the conjugated structure. In the PGz structure, due to the effect of the counter ion (bromide), the charges at the HOMO are more concentrated on the seven-membered ring, leading to an increase at the HOMO energy level by ca. 0.35 eV. At the LUMO, similar to the dedoped structure, charge delocalization is clearly observed across the entire conjugated structure. Besides, in the electron density maps of the Gz and PGz structures, it can be observed that the five-membered ring has a highly electronegative character, while the electropositive character increases in the seven-membered rings (Figure S13, Supporting Information). These results also enhance the bipolar character in the Gz and PGz structures, facilitating the S0-S1 transition in the UV–vis spectra within the visible and NIR regions,

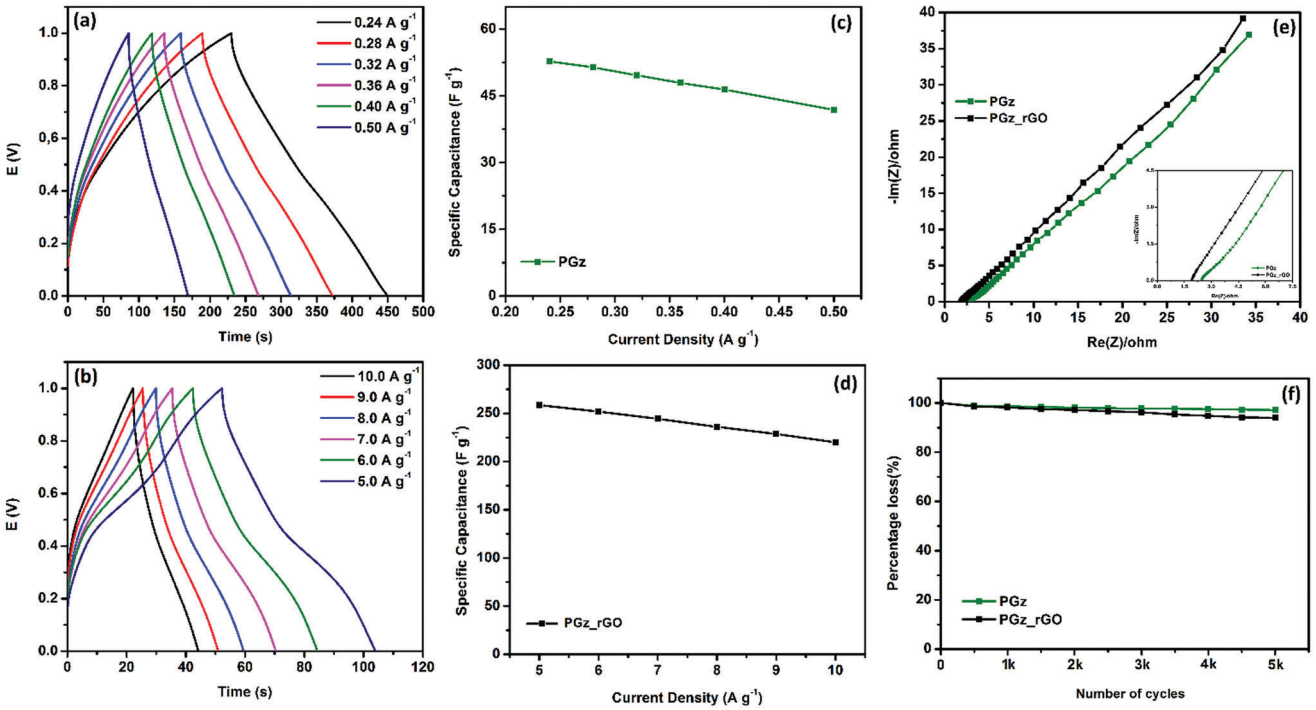

Figure 10. Galvanostatic charge and discharge (GCD) curve a) PGz electrode. b) PGz_rGO electrode. Capacitance values of c) PGz electrode and d) PGz_rGO electrode at various current densities. e) Nyquist curves of the PGz and PGz_rGO electrodes with doping modes. f) Cycling stabilities.

respectively, which is attributed to the forbidden HOMO-LUMO transition.

The capacitive performances of the PGz and PGz_rGO electrodes were assessed using cyclic voltammetry (CV) and galvanostatic charge-discharge (GCD) measurements. **Figure 9**a,b illustrate typical cyclic voltammograms of electrodes developed at different scan rates ranging from 50 to 500 mV s^{-1} within the potential range of −0.2 to 0.5 V. For all scan rates, the voltammograms are quasi-square in shape; this supports the ion-electrode pore compatibility at the electrode-electrolyte interface.[75] Although the semi-rectangular CV profiles deviate relatively from the rectangular shape at higher scan rates, due to diffusion limitations and increased transfer resistance, both CV curves exhibit ideal capacitive behavior.[76]

In addition, the CV curves reveal that the PGz_rGO electrode exhibits a significantly larger loop area compared to the PGz electrode, suggesting a higher capacitance value. This elevated capacitance in the PGz_rGO electrode is likely due to the synergistic effects within the PGz_rGO, stemming from the substantial pseudocapacitive contribution of PGz and the excellent electrical conductivity of the rGO. The interconnected structure of the PGz_rGO provides numerous diffusion channels for rapid faradaic reactions and reduces the diffusion length of electrolyte ions. Furthermore, an in-depth examination of the cyclic voltammetry profiles was conducted to observe the charge-storage mechanisms in the PGz_rGO electrode, employing the power law. The analysis of the CV data, employing the Dunn equation ($i = k_1\nu + k_2\nu^{0.5}$), allows for the determination of processes controlled by the electrical double layer (EDL) and pseudo-capacitance. Here, the first term, $k_1\nu$, signifies the current attributed to the EDL effect, whereas the second term, $k_2\nu 0.5$, represents the current linked with pseudocapacitive reactions.[77] Although the pseudo-capacitive mechanism was dominant in both electrodes, it was shown that the EDL effect increased significantly during ion doping and dedoping of PGz at increasing scan rates (Figure 8c,d). Thus, both electrodes can be regarded as hybrid SC electrodes.

Within a potential window of 0.0–1.0 V, PGz-based electrodes exhibit relatively symmetric triangular shapes at current densities ranging from 0.24 to 0.50 and 5.0 to 10.0 A g^{-1} (**Figure 10**a,b). The fact that the GCD curves are not perfectly triangular indicates that the electrodes possess higher pseudocapacitive charge storage properties compared to EDLC properties. This is particularly evident in the PGz_rGO electrode and supports the higher pseudo-capacitive contribution in PGz_rGO as calculated from the Dunn equation. The PGz electrode exhibits a specific capacitance of 52.75 F g^{-1} at a current density of 0.24 A g^{-1}, while retaining 79.3% of its initial capacitance (41.85 F g^{-1}) at 0.50 A g^{-1}. In contrast, the PGz_rGO electrode shows a specific capacitance of 258.6 F g^{-1} at a current density of 5.00 A g^{-1}, decreasing to 85.1% of its initial capacitance (220.1 F g^{-1}) at 10.0 A g^{-1} (Figure 10c,d).

The EIS technique was used to evaluate the charge-transfer resistance (R_{ct}) and the diffusion of electrolyte ions to the electrode surface (Figure 10e). The EIS spectra were analyzed over a frequency range of 1 MHz to 80 mHz to further assess the charge transport properties of the samples. The R_{ct} value, which is an important factor in evaluating the conductivity of the electrodes and is obtained from the diameter of the semicircle in the high-frequency region, was found to be lower in the PGz_rGO electrode. This indicates faster reaction kinetics and remarkable electrical conductivity due to the synergistic effect between PGz and rGO molecules and the presence of graphene oxide in the

composite. Additionally, the internal resistance (R_s), determined from the intersection of the EIS curve with the Re(Z) axis, shows that the PGz_rGO electrode has a steeper slope in the linear region compared to the other electrode, indicating greater ion diffusion to the electrode surface; the voids in the structure facilitate the transport of ions and electrons.[78] The electrochemical stability (cycling stability) of PGz and PGz_rGO electrodes was examined in 1 M H_2SO_4 aqueous electrolyte by galvanostatic CD measurements (Figure 10f) at current densities of 0.24 and 5.00 A g^{-1}. After 5000 cycles, the electrochemical retention showed a loss of only 2.9% for PGz and 6% for PGz_rGO. These results are superior to many of the previously fabricated CCP-based SC electrodes and are attributed to both nanoporous networks and high ionic density (radical cations and bromide ions) present in PGz.

3. Conclusion

Our findings outline a facile and sustainable photopolymerization method for the fabrication of a natural substance-based conjugated conductive polymer possessing remarkable SC electrode features. Especially, PGz_rGO's supercapacitor performance figures were all comparable to those of commercial supercapacitor electrodes, such as high energy density (30.57 vs ≈10–20 Wh kg^{-1}), high power density (2118.8 vs 2000–10 000 W kg^{-1}), high cycling stability (97% vs near 100% after 5000 cycles) and finally high specific capacitance (258.6 vs ≈100 F g^{-1}).[79] The superior SC properties of PGz and PGzare attributed to their high electrical/ionic conductivity, their hierarchical porous morphology, and finally the presence of strong $\pi-\pi$ interactions observed in PXRD, which are expected to play a crucial role in ion transportation. Considering the large-scale implications of the production of modern carbon-based SC electrodes, PGz can be a new edge for commercial SC electrodes. Combined with rGO which has a high surface area, PGz displayed excellent SC electrode properties including fast charge/discharge, high energy, and power densities. The PGz_rGO electrode can be a promising sustainable alternative to commercial porous carbon-based SCs. Photochemically obtained PGz displayed favorable optic properties with high molar absorption coefficients in organic solvents and also in water, making it a promising candidate for various optoelectronic applications. Moreover, considering PGz's water solubility, its absorption in the NIR region, and the previous demonstrations of the generation of reactive oxygen species (ROS) during the irradiation of guaiazulene,[80] PGz holds potential for bioapplications such as photodynamic therapy (PDT).

Supporting Information

Supporting Information is available from the Wiley Online Library or from the author.

Acknowledgements

The authors acknowledge the support from Istanbul Technical University Research Project: TGA-2024-45651 and thank to Istanbul Technical University. Sermet Koyuncu and Sinem Altınışık also acknowledge the Office of Scientific Research Projects Coordination at Çanakkale Onsekiz Mart University for infrastructure support. Grant number: FIA-2020-3312.

Conflict of Interest

The authors declare no conflict of interest.

Data Availability Statement

The data that support the findings of this study are available in the supplementary material of this article.

Keywords

conjugated conductive polymers polymers, hierarchical nanoporosity, photopolymerization, poly(guaiazulene), supercapacitor electrodes

Received: July 19, 2024
Revised: September 20, 2024
Published online: October 11, 2024

[1] A. S. Aricò, P. Bruce, B. Scrosati, J.-M. Tarascon, W. van Schalkwijk, *Nat. Mater.* **2005**, *4*, 366.
[2] T. Ibrahim, T. Kerekes, D. Sera, A. Lashab, D.-I. Stroe, *Batteries* **2024**, *10*, 42.
[3] D. C. U. Sirimanne, N. Kularatna, N. Arawwawala, *Electronics* **2023**, *12*, 2465.
[4] Y. Wu, C. Cao, *Sci. China Mater.* **2018**, *61*, 1517.
[5] J. Lang, X. Zhang, L. Liu, B. Yang, J. Yang, X. Yan, *J. Power Sources* **2019**, *423*, 271.
[6] P. Vaghela, V. Pandey, A. Sircar, K. Yadav, N. Bist, R. Kumari, *MRS Energy Sustain.* **2023**, *10*, 261.
[7] H. Zhao, L. Liu, R. Vellacheri, Y. Lei, *Adv. Sci.* **2017**, *4*, 1700188.
[8] J. M. Lim, Y. S. Jang, H. Van, T. Nguyen, J. S. Kim, Y. Yoon, B. J. Park, D. H. Seo, K.-K. Lee, Z. Han, K. Ostrikov, S. G. Doo, *ACS Appl. Mater. Interfaces* **2023**, *5*, 615.
[9] C. An, Y. Zhang, H. Guo, Y. Wang, *Nanoscale Adv.* **2019**, *1*, 4644.
[10] S. Kumar, M. A. Rehman, S. Lee, M. Kim, H. Hong, J.-Y. Park, Y. Seo, *Sci. Rep.* **2021**, *11*, 649.
[11] Z. Zhai, L. Zhang, T. Du, B. Ren, Y. Xu, S. Wang, J. Miao, Z. Liu, *Mater. Des.* **2022**, *221*, 111017.
[12] T. Liu, L. Finn, M. Yu, H. Wang, T. Zhai, X. Lu, Y. Tong, Y. Li, *Nano Lett.* **2014**, *14*, 2522.
[13] S.-J. Shin, J. W. Gittins, C. J. Balhatchet, A. Walsh, A. C. Forse, *Adv.Funct. Mater.* **2023**, 2308497.
[14] A. Velasco, Y. K. Ryu, A. Boscá, A. Ladrón-de-Guevara, E. Hunt, J. Zuo, J. Pedrós, F. Calle, J. Martinez, *Sustain. Energy Fuels* **2021**, *5*, 1235.
[15] L. F. Aval, M. Ghoranneviss, G. B. Pour, *Heliyon* **2018**, *4*, 00862.
[16] H. Wang, X. Yan, G. Piao, *Electrochim. Acta* **2017**, *231*, 264.
[17] A. G. Olabi, Q. Abbas, M. A. Abdelkareem, A. H. Alami, M. Mirzaeian, E. T. Sayed, *Batteries* **2023**, *9*, 19.
[18] Z. Li, Q. Liu, L. Sun, N. Li, X. Wang, Q. Wang, D. Zhang, B. Wang, *Chem. Eng. Sci.* **2022**, *252*, 117514.
[19] B. Chen, D. Wu, T. Wang, F. Yuan, D. Jia, *Chem. Eng. J.* **2023**, *462*, 142163.
[20] L. Szabó, X. Xu, K. Uto, J. Henzie, Y. Yamauchi, I. Ichinose, M. Ebara, *ACS Appl. Mater. Interfaces* **2022**, *14*, 4004.
[21] Q. Huang, J. Chen, S. Yan, X. Shao, Y. Dong, J. Liu, W. Li, C. Zhang, *ACS Sustain. Chem. Eng.* **2021**, *9*, 13807.
[22] M. G. Say, C. J. Brett, J. Edberg, S. V. Roth, L. D. Söderberg, I. Engquist, M. Berggren, *ACS Appl. Mater. Interfaces* **2022**, *14*, 55850.
[23] G. A. Snook, P. Kao, A. S. Best, *J. Power Sources* **2011**, *196*, 1.
[24] M. Suominen, S. Lehtimäki, R. Yewale, P. Damlin, S. Tuukkanen, C. Kvarnström, *J. Power Sources* **2017**, *356*, 181.

[25] R. P. Steer, *J. Photochem. Photobiol., C* **2019**, *40*, 68.
[26] R. Yewale, P. Damlin, M. Suominen, C. Kvarnström, *Mater. Chem. Phys.* **2022**, *275*, 125292.
[27] J. Xiang, D. Vu, M. He, C. Duan, C. Ge, C. R. McNeill, X. Gao, *Macromolecules* **2023**, *56*, 9475.
[28] Z. Zhao, W. Huan, C. Sun, M. E. El-Khouly, B. Zhang, Y. Chen, *New J. Chem.* **2022**, *46*, 3800.
[29] R. Rieger, K. Müllen, *J. Phys. Org. Chem.* **2010**, *23*, 315.
[30] S. B. Mdluli, M. E. Ramoroka, S. T. Yussuf, K. D. Modibane, V. S. John-Denk, E. I. Iwuoha, *Polymers* **2022**, *14*, 716.
[31] I. T. Horváth, *Chem. Rev.* **2018**, *118*, 369.
[32] F. Torricelli, I. Alessandri, E. Macchia, I. Vassalini, M. Maddaloni, L. Torsi, *Adv. Mater. Technol.* **2022**, *7*, 2100445.
[33] R. Madhu, A. P. Periasamy, P. Schlee, S. Hérou, M.-M. Titirici, *Carbon* **2023**, *207*, 172.
[34] B. K. Roy, I. Tahmid, T. U. Rashid, *J. Mater. Chem. A* **2021**, *9*, 17592.
[35] O. Boujibar, A. Ghosh, O. Achak, T. Chafik, F. Ghamouss, *J. Energy Storage* **2019**, *26*, 100958.
[36] M. Hoseinizadeh, K. E. Salem, A. Gouda, D. Belanger, C. Santato, *Waste Biomass Valor.* **2023**, *14*, 3475.
[37] X. Lin, Y. Xu, J. Wu, J. Huang, *Nanoscale Adv.* **2022**, *4*, 1445.
[38] M. Ganesapillai, R. Mehta, A. Tiwari, A. Sinha, H. S. Bakshi, V. Chellappa, J. Drewnowski, *Heliyon* **2023**, *9*, 14873.
[39] S. Dadashi-Silab, S. Doran, Y. Yagci, *Chem. Rev.* **2016**, *116*, 10212.
[40] X. Luo, J. Wan, N. Meckbach, V. Strehmel, S. Li, Z. Chen, B. Strehmel, *Angew. Chem., Int. Ed.* **2022**, *61*, 202208180.
[41] Q. Wang, S. Popov, A. Feilen, V. Strehmel, B. Strehmel, *Angew. Chem., Int. Ed.* **2021**, *60*, 26855.
[42] H. Zou, H. Schlaad, *J. Polym. Sci., A: Polym. Chem.* **2015**, *53*, 1260.
[43] K. Kaya, T. Debsharma, H. Schlaad, Y. Yagci, *Polym. Chem.* **2020**, *11*, 6884.
[44] Z. Zhang, N. Corrigan, A. Bagheri, J. Jin, C. Boyer, *Angew. Chem., Int. Ed.* **2019**, *58*, 17954.
[45] E. F. Woods, A. J. Berl, J. A. Kalow, *ChemPhotoChem* **2021**, *5*, 4.
[46] K. Kaya, *React. Funct. Polym.* **2023**, *182*, 105464.
[47] T. Tabak, K. Kaya, R. Isci, T. Ozturk, Y. Yagci, B. Kiskan, *Macromol. Rapid Commun.* **2024**, *45*, 2300455.
[48] T. Tabak, S. Altinisik, S. Ulucay, S. Koyuncu, K. Kaya, *Macromolecules* **2024**, *57*, 4769.
[49] K. Kaya, E. A. Alkan, M. Yasa, A. Süerkan, Y. A. Udum, L. Toppare, Y. Yagci, *Eur. Polym. J.* **2021**, *161*, 110831.
[50] K. Kaya, S. Koyuncu, Y. Yagci, *Chem. Commun.* **2019**, *55*, 11531.
[51] E. Sari, G. Yilmaz, S. Koyuncu, Y. Yagci, *J. Am. Chem. Soc.* **2018**, *140*, 12728.
[52] A. Kocaarslan, K. Kaya, S. Jockusch, Y. Yagci, *Angew. Chem., Int. Ed.* **2022**, *61*, 202208845.
[53] T. Celiker, K. Kaya, S. Koyuncu, Y. Yagci, *Macromolecules* **2020**, *53*, 5787.
[54] G. E. Williams, G. Kociok-Köhn, T. D. James, S. E. Lewis, *Org. Biomol. Chem.* **2021**, *19*, 2502.
[55] S. K. Prajapat, C. Subramani, P. Sharma, S. Vrati, M. Kalia, *Autophagy Rep.* **2022**, *1*, 523.
[56] D. Bilger, K.-W. Park, A. Abdel-Maksoud, T. L. Andrew, *Polym. Chem.* **2020**, *11*, 7656.
[57] T. P. A. van der Pol, S. T. Keene, B. W. H. Saes, S. C. J. Meskers, A. Salleo, Y. van de Burgt, R. A. J. Janssen, *J. Phys. Chem. C* **2019**, *123*, 24328.
[58] Y. Inoue, I. Shinohara, I. Murata, I. Kanamoto, *J. Mol. Struct.* **2019**, *1186*, 50.
[59] T. Ghosh, J. S. Panicker, V. C. Nair, *Polymers* **2017**, *9*, 112.
[60] Y. Liu, Y. Ma, S. Guang, H. Xu, X. Su, *J. Mater. Chem. A* **2014**, *2*, 813.
[61] T. Shida, S. Iwata, *J. Am. Chem. Soc.* **1973**, *95*, 3473.
[62] E. H. Suh, J. G. Oh, J. Jung, S. H. Noh, T. S. Lee, J. Jang, *Adv. Energy Mater.* **2020**, *10*, 2002521.
[63] T. Gözet, A. M. Önal, J. Hacaloglu, *J. Macromol. Sci., Part A: Pure Appl. Chem.* **2007**, *44*, 259.
[64] R. Luque, A. Ahmad, S. Tariq, M. Mubashir, M. Sufyan Javed, S. Rajendran, R. S. Varma, A. Ali, C. Xia, *Mater. Today* **2024**, *73*, 105.
[65] K. Surya, M. S. Michael, *J. Electroanal. Chem.* **2020**, *878*, 114674.
[66] O. Barbieri, M. Hahn, A. Herzog, R. Kötz, *Carbon* **2005**, *43*, 1303.
[67] M. Kroupa, G. J. Offer, J. Kosek, *J. Electroanal. Chem.* **2016**, *163*, A2475.
[68] M. Sevilla, A. B. Fuertes, *ACS Nano* **2014**, *8*, 5069.
[69] T. Tsuchiya, T. Hamano, M. Inoue, T. Nakamura, A. Wakamiya, Y. Mazaki, *Chem. Commun.* **2023**, *59*, 10604.
[70] A. Kumorkiewicz-Jamro, R. Górska, M. Krok-Borkowicz, P. Mielczarek, Ł. Popenda, K. Lystvan, E. Pamuła, S. Wybraniec, *J. Agric. Food Chem.* **2023**, *71*, 15017.
[71] X. Wang, J. K.-P. Ng, P. Jia, T. Lin, C. M. Cho, J. Xu, X. Lu, C. He, *Macromolecules* **2009**, *42*, 5534.
[72] T. Makinoshima, M. Fujitsuka, M. Sasaki, Y. Araki, O. Ito, S. Ito, N. Morita, *J. Phys. Chem. A* **2004**, *108*, 368.
[73] R. S. H. Liu, A. E. Asato, *J. Photochem. Photobiol., C* **2003**, *4*, 179.
[74] J. Huang, S. Huang, Y. Zhao, B. Feng, K. Jiang, S. Sun, C. Ke, E. Kymakis, X. Zhuang, *Small Methods* **2020**, *4*, 2000628.
[75] H. Xin, B. Hou, X. Gao, *Acc. Chem. Res.* **2021**, *54*, 1737.
[76] N. H. N. Azman, M. S. Mamat @ Mat Nazir, L. H. Ngee, Y. Sulaiman, *Int. J. Energy Res.* **2018**, *42*, 2104.
[77] H. Qin, P. Liu, C. Chen, H.-P. Cong, S.-H. Yu, *Nat. Commun.* **2021**, *12*, 4297.
[78] J. Wang, J. Polleux, J. Lim, B. Dunn, *J. Phys. Chem. C* **2007**, *111*, 14925.
[79] D. C. U. Sirimanne, N. Kularatna, N. Arawwawala, *Electronics* **2023**, *12*, 2465.
[80] H.-M. Chiang, J.-J. Yin, Q. Xia, Y. Zhao, P. P. Fu, K.-C. Wen, H. Yu, *J. Photochem. Photobiol., A* **2010**, *211*, 123.